Available online at www.sciencedirect.com
ScienceDirect
Trans. Nonferrous Met. Soc. China 32(2022) 3550−3562
Transactions of Nonferrous Metals Society of China
www.tnmsc.cn

Effects of pre-compression on formation of dynamic precipitates and creep anisotropy of hot-extruded AZ91−2Y magnesium alloy

Wei LI[1], Huang HUANG[1], Wei-ying HUANG[1], Jian CHEN[1], Sheng-de ZHANG[2], Zhen-yu XIAO[3], Wei QIU[1]

1. Key Laboratory of Efficient & Clean Energy Utilization, School of Energy and Power Engineering, Changsha University of Science & Technology, Changsha 410114, China;
2. Japan Electric Power Central Research Institute, Tokyo 240-0196, Japan;
3. State Key Laboratory of Advanced Design and Manufacturing for Vehicle Body, Hunan University, Changsha 410082, China

Received 8 September 2021; accepted 25 March 2022

Abstract: The creep anisotropy behavior under different stresses at 180 °C of hot-extruded AZ91−2Y magnesium alloy with pre-compression (PC) and without pre-compression (NPC) was studied. Microstructure, texture and mechanical properties of the alloy were examined by scanning electron microscopy (SEM), electron backscatter diffraction (EBSD), transmission electron microscopy (TEM) and tensile creep tests. The results revealed that the creep resistance was proportional to the volume fraction of spherical $Mg_{17}Al_{12}$ precipitates. The dynamic precipitation of large volume fraction of lamellar $Mg_{17}Al_{12}$ in NPC samples leads to the basal $\langle a \rangle$ slip as the dominant creep mechanism, and the NPC samples have obvious anisotropy. In the PC samples, dynamic precipitation of large volume fraction of spherical $Mg_{17}Al_{12}$ has inhibitory effect on the basal $\langle a \rangle$ slip. The pyramidal $\langle c+a \rangle$ slip and twinning improve the creep anisotropy resistance significantly.

Key words: magnesium alloy; creep anisotropy; pre-compression; twin; dislocation

1 Introduction

AZ91 Mg alloys are widely used in aerospace and automotive industry owing to their high specific strength [1−3]. However, the basal texture and the onset of β-$Mg_{17}Al_{12}$ dynamic precipitates with a lamellar morphology and spherical structure at 150−350 °C results in basal and other slips with different activities depending on the loading modes [4−7]. As a result, AZ91 Mg alloys show high creep anisotropy, which limits the current applications of these materials. The addition of rare earth elements can reduce the formation of precipitates in Mg alloys, thereby favoring non-basal slip and reducing the anisotropy [8−11]. In this sense, the addition of a rare earth such as yttrium (Y) to Mg alloys can change the basal and non-basal slips as well as the twinning activities, thereby changing the creep mechanism and creep properties [12]. For example, ZHANG et al [13] found that the pyramidal $\langle c+a \rangle$ slip introduced in Mg−5.5wt.%Y alloy resulted in strain hardening during the creep process, allowing the alloy to show excellent creep resistance in both the rolling and transverse directions (RD and TD, respectively). LU et al [14] showed that a higher proportion of non-basal slip systems were activated at 300 °C for Mg−5wt.%Y as compared to Mg−1wt.%Y, with the former showing superior yield strength anisotropy. Nevertheless, it is difficult to avoid anisotropy completely in Mg−Y alloys, especially with a low content of Y. In addition, anisotropy is influenced by the type of $Mg_{17}Al_{12}$ precipitates formed [15].

Corresponding author: Wei-ying HUANG, Tel: +86-17775990204, E-mail: huangwy@csust.edu.cn
DOI: 10.1016/S1003-6326(22)66038-2
1003-6326/© 2022 The Nonferrous Metals Society of China. Published by Elsevier Ltd & Science Press

Depending on the precipitation mechanism, two kinds of precipitates are formed in the AZ series of Mg alloys, namely, lamellar and spherical-structured precipitates [5,15−17]. JIANG et al [18] studied the high-temperature creep resistance of AZJ911 alloy and found two kinds of precipitates formed during the creep test. They pointed out that a strong stress concentration on the lamellar $Mg_{17}Al_{12}$ precipitate deteriorated the creep properties, while spherical $Mg_{17}Al_{12}$ showed a higher deformation resistance. SRINIVASAN et al [5] revealed that the coarsening of lamellar $Mg_{17}Al_{12}$ had limited effect on pinning both dislocations and boundaries, resulting in a poor creep resistance at later stages. ZHA et al [19] investigated the effect of the volume fraction of spherical $Mg_{17}Al_{12}$ on the tensile behavior of Mg alloys, and they found that a high volume fraction of spherical structure can transform grain boundaries effectively. Thus, reducing the amount of lamellar $Mg_{17}Al_{12}$ or increasing the volume fraction of spherical $Mg_{17}Al_{12}$ can be used to enhance the creep resistance and improve the creep anisotropy of AZ series Mg alloys. JIANG et al [20] used equal-channel angular extrusion technology to pre-deform and machine remelted AZ61 Mg alloys, obtaining a high volume fraction of spherical $Mg_{17}Al_{12}$ semisolid billets. XU et al [21] machined an AZ91D Mg alloy through a repetitive upsetting–extrusion process, and found a structure containing highly spherical $Mg_{17}Al_{12}$ precipitates. However, the complex machining process limits the applications of this method.

In recent years, twins introduced by pre-deformation have received considerable attentions as a method to improve the mechanical properties of alloys [22−24]. SHI et al [25] found that pre-compression activated both large amounts of classical and concomitant $\{10\bar{1}2\}$ twins in hot-rolled Mg−4Y binary alloys. A cross-slip was successfully inhibited by the concomitant $\{10\bar{1}2\}$ twin boundaries, while pyramidal $\langle c+a\rangle$ slip dominated the creep process of pre-compression samples. CHEN et al [26] discovered that pre-twinning led to a hardening effect in an AZ31 Mg alloy, resulting in a higher yield stress compared to non-extruded samples. Furthermore, pre-deformation can induce noticeable effects on the anisotropy of these alloys. XIAO et al [27] successfully enhanced the creep anisotropy of a hot-extruded Mg−2Y alloy by presetting the twins to suppress the dislocation slip. Despite these advances, the published studies are either aimed at enhancing the creep properties or reducing the anisotropy of Mg alloys. The effect of twinning on the volume fraction of different dynamic precipitates has been scarcely studied in the literature. In addition, the improvement of the creep properties and anisotropy of these alloys by pre-deformation still remains to be solved.

In the present work, tensile creep tests along the extrusion direction (ED) and TD of an AZ91−2Y alloy with and without pre-deformation were carried out at 180 °C under varying applied stresses. This study was aimed to ascertain the effects of twins introduced by compression on the formation of dynamic precipitates and the creep anisotropy. We believe that this work can provide a valid method to maximize creep resistance and decrease the anisotropy of low-RE AZ series magnesium alloys, and meanwhile provide a reference for the application of AZ magnesium alloys in high-temperature automobile parts (such as gearbox body).

2 Experimental

The AZ91−2Y alloy used herein was obtained by the method of water-cooling semi-continuous casting. The cast ingots were prepared by melting pure Mg (99.9%), pure Al (99.9%), pure Zn (99.9%), and Mg−33.3wt.%Y master alloy. The resulting alloys were machined into cylindrical specimens of 250 mm in length and 168 mm in diameter. After being heated at 400 °C for 12 h, the specimens was extruded at 400 ºC with an extrusion ratio of 16:1 at an extrusion speed of ~17 mm/s. The extruded bar was cut into dimensions of 30 mm in length along the ED at room temperature (RT). The bars were then solution-treated at 380 °C for 5 h, followed by quenching in water. A compressive straining of 0.05 along the ED (thickness reduction of 5%) was applied on a part of the solution-treated bars with a strain rate of 1×10^{-3} s^{-1} at RT. A schematic diagram of the preparation method and the dimension of samples is shown in Fig. 1.

All samples were dog-bone shaped, and the tensile direction was either TD or ED. For convenience, the solution-treated (NPC) and pre-compression (PC) after solution-treated samples

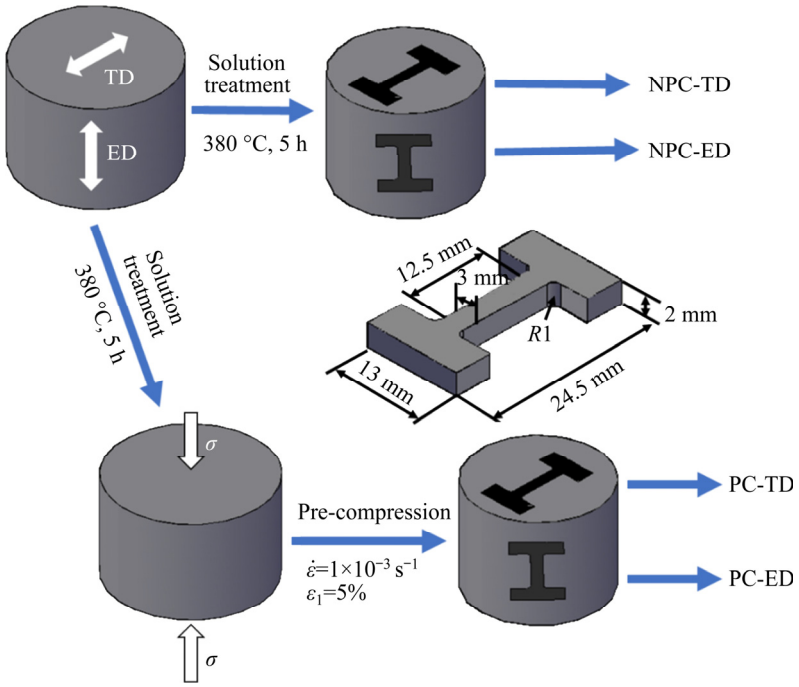

Fig. 1 Schematic diagram of preparation method and dimension of samples

were labeled as PC sample, and NPC sample, respectively. Creep tests were performed at 180 °C under constant applied stresses ranging from 50 to 70 MPa with a crosshead speed of 0.04 mm/min (initial strain rate of 3.75×10^{-5} s^{-1}). Before carrying out the elevated-temperature tensile or the creep tests, the samples were heated to 180 °C and hold at this temperature for 30 min until the temperature in each sample was uniform and stable.

The microstructure and texture evolutions were followed by scanning electron microscopy (SEM), and electron backscatter diffraction (EBSD). Transmission electron microscopy (TEM) was used to observe the internal microstructures. The OM samples were first mechanically ground with 1200$^{\#}$, 2000$^{\#}$, and 3000$^{\#}$ abrasive papers, polished with an Al_2O_3 polishing agent and finally etched in a solution containing 2 g of oxalic acid, 1 mL of nitric acid, 2 mL of acetic acid and 100 mL distilled water. The samples for TEM observations were prepared by cutting a disk of 3 mm in diameter, which was mechanically ground to a thickness of 80 μm and finally ion-milled to perforation.

3 Results

3.1 Microstructures before creep

Figure 2 shows typical orientation imaging microscopy (OIM) graphs and the corresponding {0001} pole graphs of the initial NPC and PC samples. As shown in Fig. 2(a), the basal colors of NPC samples were blue and green, with an average grain size of about 80 μm. These results indicated that the basal plane of the material was parallel to the ED direction. After pre-compression (Fig. 2(b)), numerous twins appeared in the samples. Most of these twins were arranged parallel to the single crystal particles, and some were arranged in cross shape. The grain size of the SP samples remained unchanged, revealing that the main effect of pre-compression was to introduce twins into the sample in advance. The {0001} pole graph of the NPC (Fig. 2(c)) and PC (Fig. 2(d)) samples revealed a typical fiber texture. Due to the introduction of twins, the relative maximum strength of the matrix texture increased from 15.461 to 17.311.

3.2 Uniaxial tensile properties

The true stress−strain curves of PC and NPC samples obtained from uniaxial tensile tests at 180 °C are shown in Fig. 3, and the uniaxial tensile properties are listed in Table 1. The yield stress of NPC-TD, NPC-ED, PC-TD and PC-ED are 53, 76, 72 and 85MPa, respectively. It can be seen that the tensile curve has obvious correlation with the

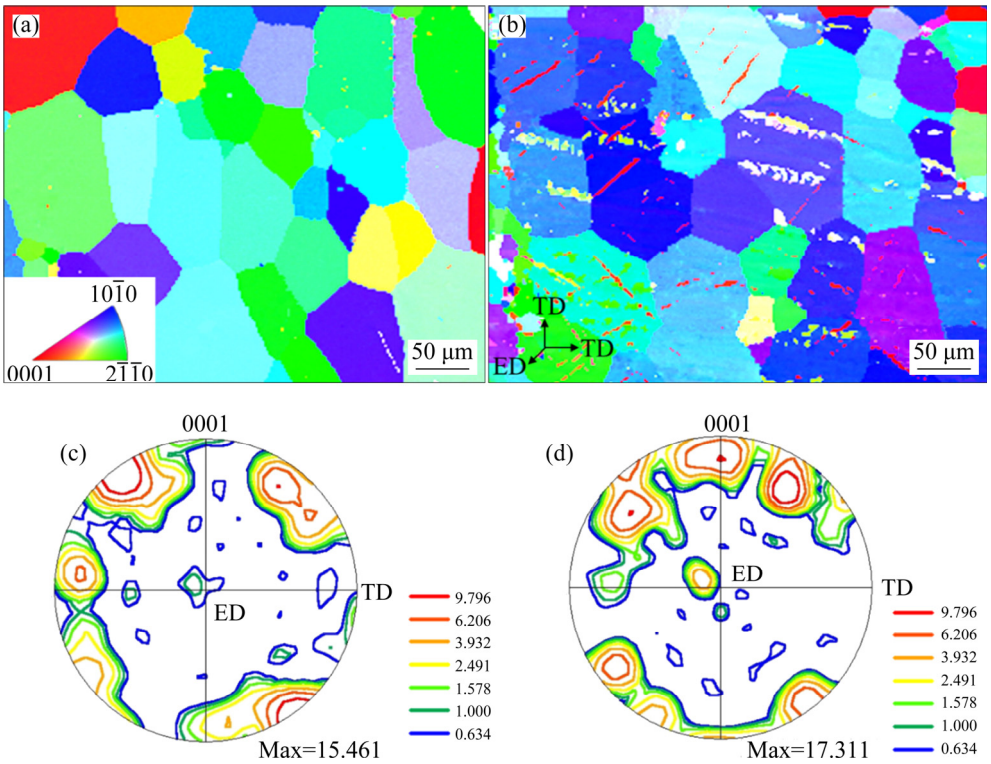

Fig. 2 Typical OIM graphs (a, b) and corresponding {0001} pole graphs (c, d) of initial NPC (a, c) and PC (b, d) samples

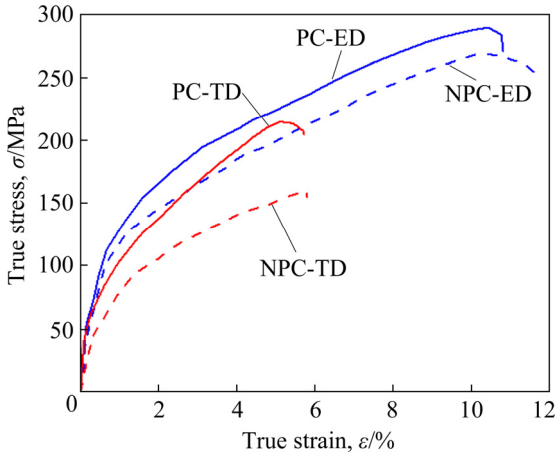

Fig. 3 True stress−strain curves obtained from uniaxial tensile tests along different directions at 180 °C

Table 1 Yield strength, ultimate tensile strength and fracture elongation measured by uniaxial tensile tests at 180 °C

Sample	Yield strength/MPa	Ultimate tensile strength/MPa	Fracture elongation/%
NPC-ED	76	265	12.1
NPC-TD	53	160	5.9
PC-ED	85	290	10.8
PC-TD	72	215	5.7

loading direction, and the NPC samples have an obvious mechanical anisotropy. After pre-compression, the mechanical properties of PC-TD sample were improved, and the anisotropy of PC samples was weakened. Note that due to the short duration of tensile test, there are almost no precipitates in the samples, so the influence of dynamic precipitates on the anisotropy during creep cannot be reflected in uniaxial tensile test.

3.3 Tensile creep properties

According to the yield strength of the samples, the tensile creep tests were carried out at varying stresses (50, 60 and 70 MPa) on the four samples studied. Figure 4 shows the typical creep strain versus time curves for the PC and NPC samples crept along the TD and ED directions (180 °C, 60 MPa). NPC samples showed a noticeable creep anisotropy, with NPC-TD showing the highest steady creep rate among the samples studied. As a result, this sample was fractured quickly and showed a creep life less than 45 h. After pre-compression, the PC samples only showed the primary and steady stages in 45 h of experiment, revealing an improved creep anisotropy. The creep

curves of the PC-TD and PC-ED samples showed similar trends, suggesting equivalent creep resistance at this stage. Furthermore, as a result of pre-compression, the PC samples showed lower creep strains and a better creep resistance compared with the NPC samples.

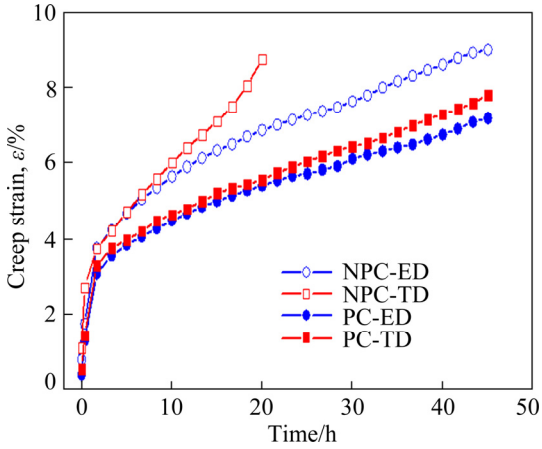

Fig. 4 Typical creep strain versus time curves of PC and NPC samples crept at 180 °C under 60 MPa

The steady creep rates of all samples under varying applied stresses are summarized in Table 2. As can be seen, the steady creep rate increased and the creep resistance decreased with the applied stress. At elevated temperatures, the steady creep rate as a function of the stress (σ) and temperature (T) is generally described by the following equation [28,29]:

$$\dot{\varepsilon} = A\sigma^n \exp(-\frac{Q}{RT}) \quad (1)$$

where A is a material constant, σ is the applied stress, n is the stress exponent, Q is the activation energy for creeping, R is the molar gas constant, and T is the thermodynamic temperature. In the present study, the temperature remains unchanged, and n can be attained by Eq. (2):

$$n = \left(\frac{\partial \ln \dot{\varepsilon}_{\min}}{\partial \ln \sigma}\right)_T \quad (2)$$

Figure 5 shows the stress exponent n obtained from the slope of a ln−ln plot of the steady creep rate versus the applied stress of the four samples. Normally, the stress exponent can respond differently to dominant creep mechanisms (n=1, 2, and 3−7 for diffusional creep, grain boundary sliding dominated creep, and dislocation movement dominated creep, respectively). When n is 7−8, the power-law breakdown happens, as a result of cross-slip in precipitation-hardened alloys or long-range plastic strain [23,30,31]. In this work, we found several stress exponents for the different samples at the same stress range (1.6, 2.4, and 2.2 for PC-ED, PC-TD and NPC-ED, respectively). The dominant mechanism in all cases was grain boundary sliding. For the NPC-TD sample, the stress exponent n was 3.9, and dislocation slip became the main deformation mechanism. In order to study the creep mechanism accurately, SEM and TEM observations were performed after the test.

Table 2 Values of steady creep rate measured by creep tests at 180 °C (s^{-1})

Sample	50 MPa	60 MPa	70 MPa
NPC-ED	1.49×10^{-5}	3.25×10^{-5}	5.90×10^{-5}
NPC-TD	4.28×10^{-5}	7.40×10^{-5}	1.20×10^{-4}
PC-ED	6.70×10^{-6}	1.91×10^{-5}	3.74×10^{-5}
PC-TD	1.48×10^{-5}	3.52×10^{-5}	6.31×10^{-5}

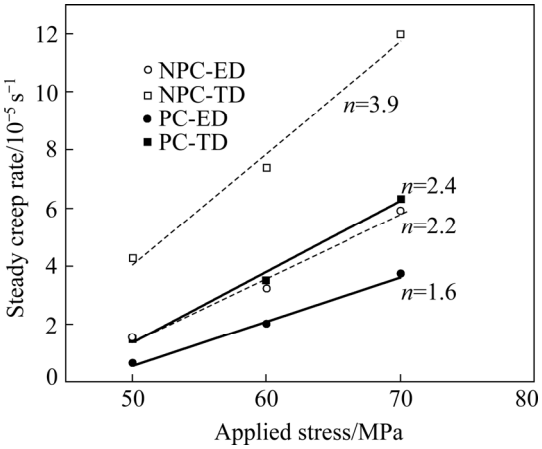

Fig. 5 Variation of steady creep rate versus applied stress at 180 °C for PC and NPC samples to calculate stress exponent n

4 Discussion

4.1 Microstructure after creep

SEM examinations were carried out to investigate the microstructure evolutions of the PC and NPC samples after creep test at 180 °C and 60 MPa (Fig. 6). Two kinds of precipitates were found in the samples, namely Al_2Y (block-shaped and sparsely distributed in the alloy) and dynamic precipitates β-$Mg_{17}Al_{12}$ (with lamellar and spherical structure clearly from the magnified view Figs. 6(f, g)). For NPC samples, lamellar $Mg_{17}Al_{12}$

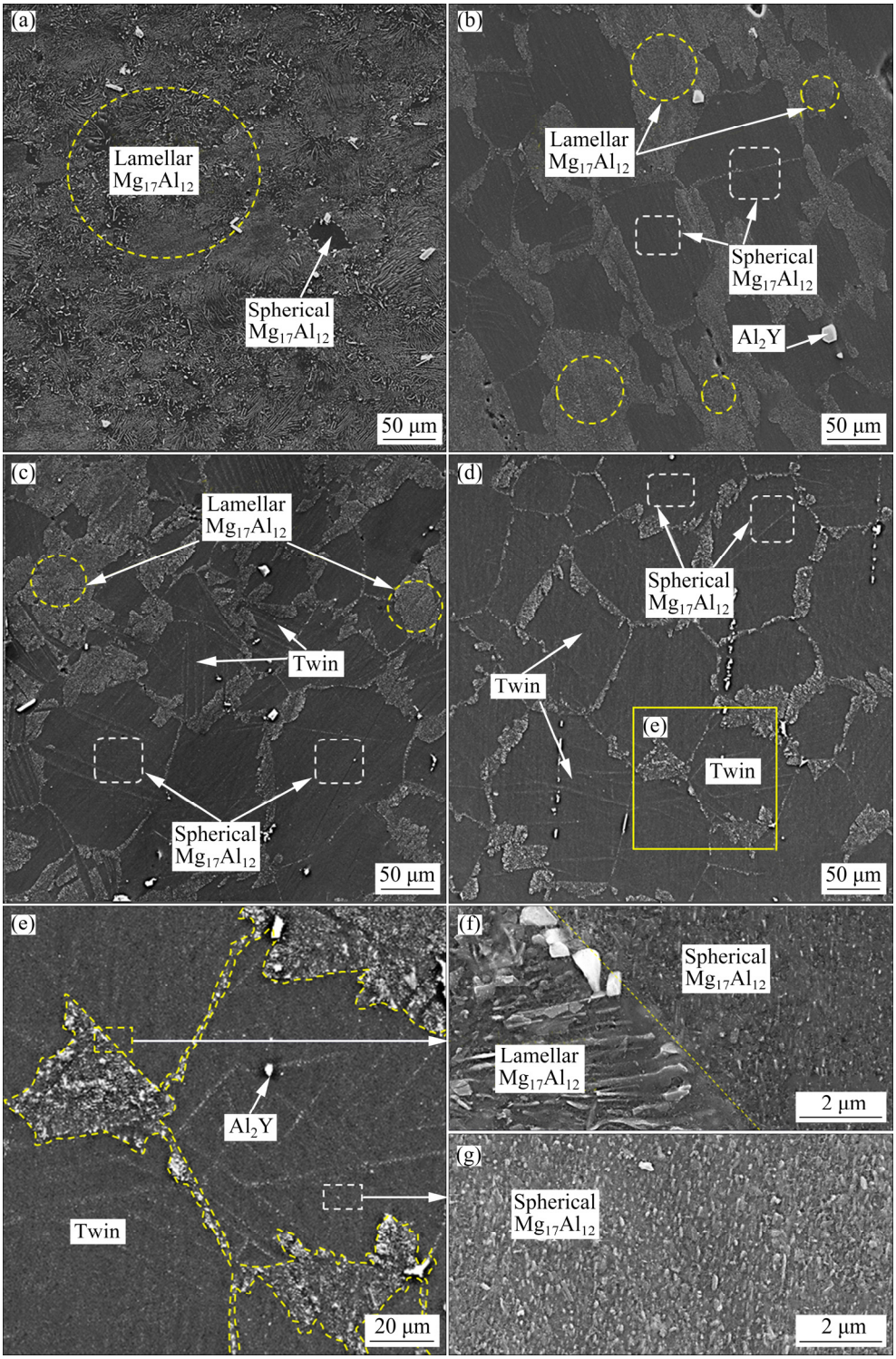

Fig. 6 SEM images of four samples after creep under 60 MPa at 180 °C: (a) NPC-TD sample; (b) NPC-ED sample; (c) PC-TD sample; (d, e, f, g) PC-ED sample

almost covered the entire surface of the NPC-TD sample (Fig. 6(a)), while the volume fraction of this precipitate in the NPC-ED sample (Fig. 6(b)) decreased significantly. In the NPC-ED samples, lamellar $Mg_{17}Al_{12}$ was more inclined to grain boundary aggregation. MAO et al [10] showed that large strain and dislocation during creep would accelerate the precipitation process. In this study, the NPC samples had creep anisotropy. As shown in Fig. 7, the average basal slip Schmidt factor of the NPC-TD sample before creep (0.329) was larger than that of the NPC-ED sample (0.188).

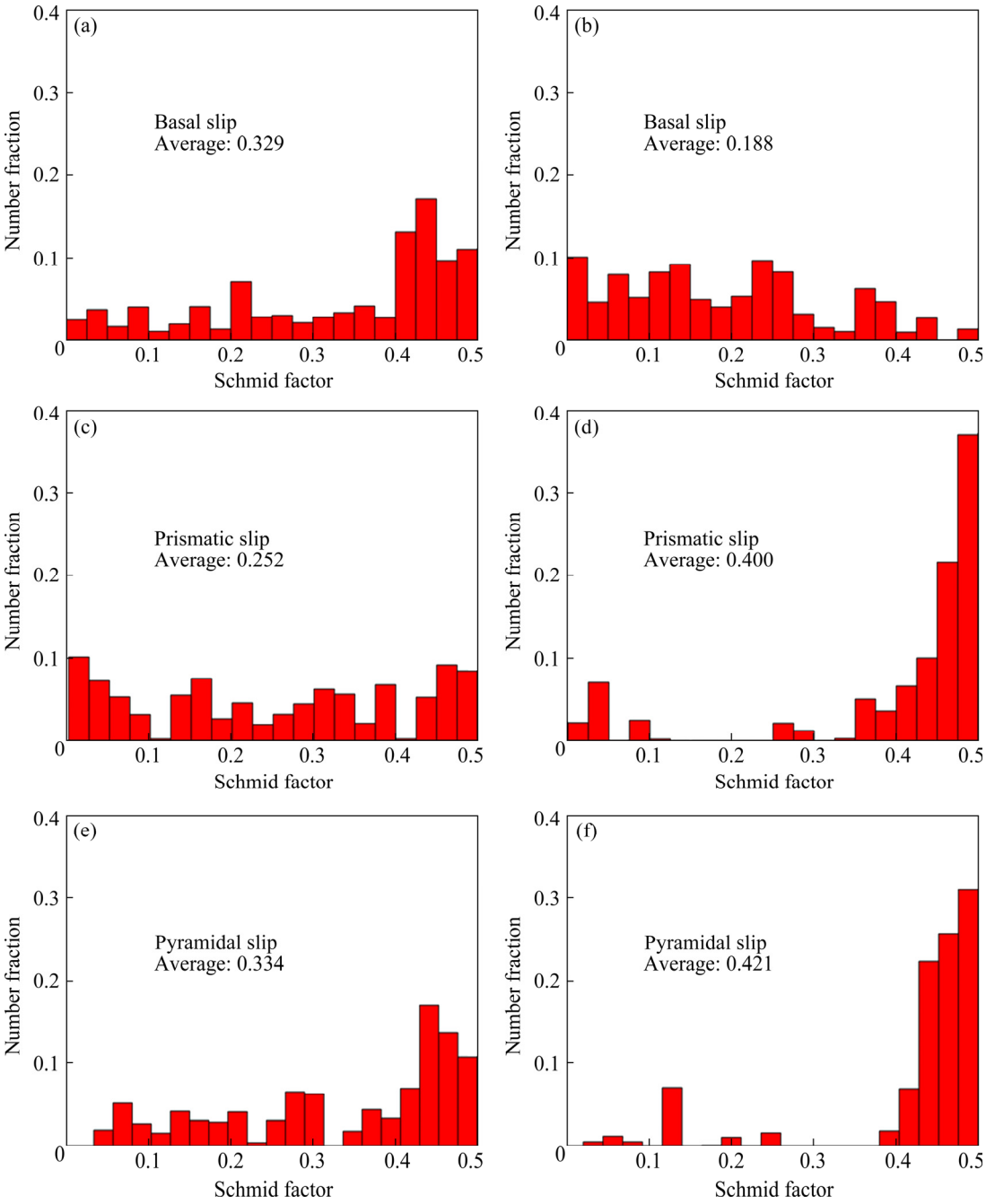

Fig. 7 Schmid factor distribution maps for NPC samples: (a, c, e) NPC-TD samples; (b, d, f) NPC-ED samples

Therefore, creep in the NPC-TD sample was dominated by basal slip, which was easier to deform than the NPC-ED sample (non-basal slip) [32]. In this case, the basal slip provided an effective diffusion path for dissolved atoms, with lamellar $Mg_{17}Al_{12}$ being easier to precipitate in the basal slip direction. Therefore, the volume fraction of lamellar $Mg_{17}Al_{12}$ in NPC-TD sample was higher than that in NPC-ED sample.

Figures 6(c, d) present the microstructures of PC samples. Obviously, the volume fraction of lamellar $Mg_{17}Al_{12}$ decreased significantly as compared to NPC samples, especially PC-TD sample. Furthermore, the volume fraction of spherical $Mg_{17}Al_{12}$ increased in these samples, precipitating mainly in the grain interior and twins. Based on the Schmidt factor distribution of the PC samples before creep (Fig. 8), the average basal slip Schmidt factor values of PC-TD and PC-ED specimens were 0.325 and 0.151, respectively. These values were not significantly different from those of the NPC specimens. However, the volume

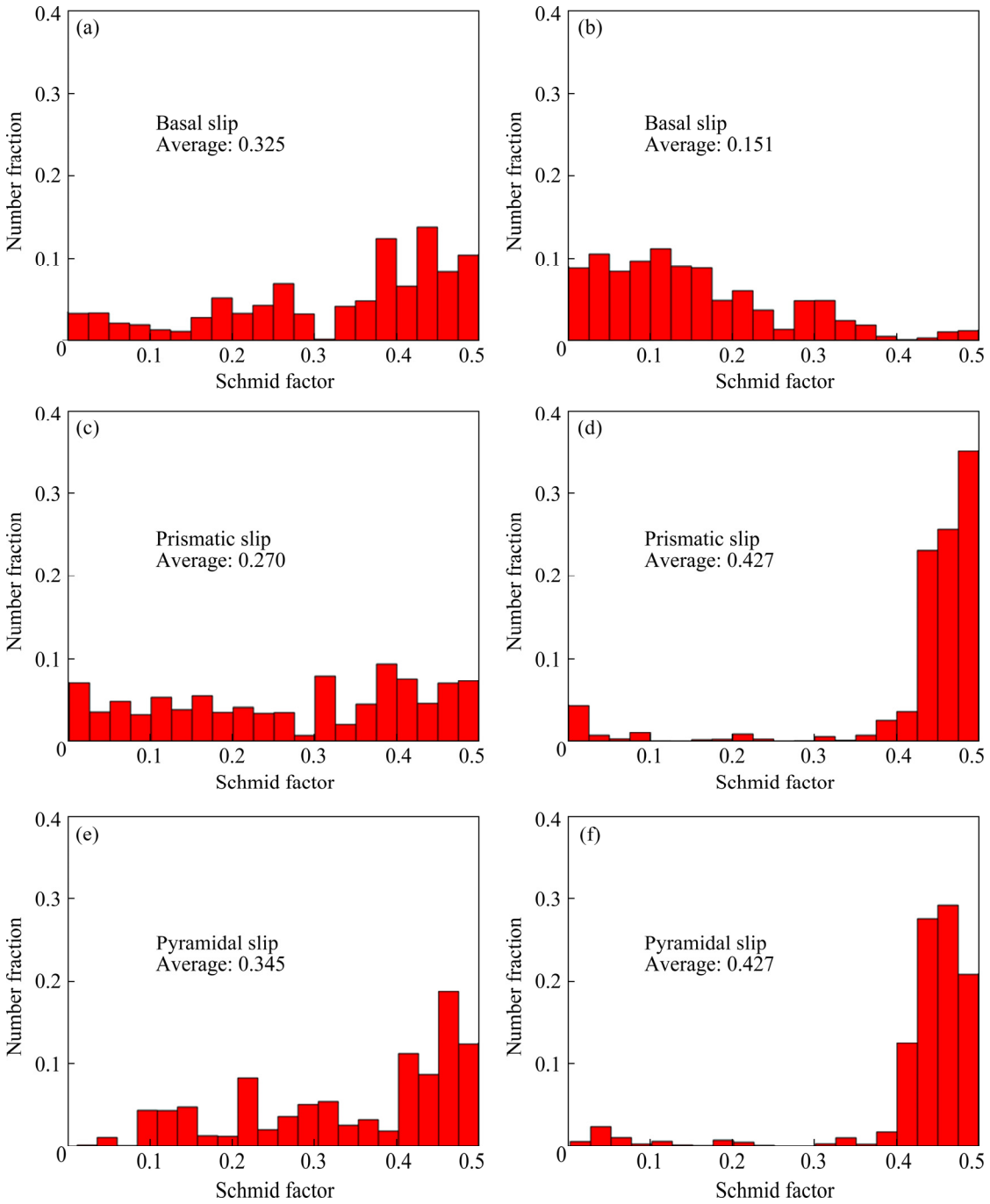

Fig. 8 Schmid factor distribution maps for PC samples: (a, c, e) PC-TD samples; (b, d, f) PC-ED samples

fraction of lamellar $Mg_{17}Al_{12}$ in the PC-TD sample was significantly reduced. Undoubtedly, this phenomenon cannot be explained only by considering the Schmidt law, and other creep mechanisms need to be included. ZHANG et al [33] introduced the twins into the Mg−4Y alloy, finding dislocation climb and frequent twin intersection became the dominant mechanism of creep, which significantly improved the creep resistance of the sample in the RD direction and played a role in improving the creep anisotropy. Based on this, we believe that the twins produced by pre-compression play an important role in the generation of the precipitation morphology during the creep process and the twinning hindering dislocations and effectively cutting off the diffusion paths of dissolved atoms. There is a competitive relationship between lamellar $Mg_{17}Al_{12}$ and spherical $Mg_{17}Al_{12}$ precipitates. Under the combined action of dislocation and temperature, the amount of

spherical $Mg_{17}Al_{12}$ increased in PC samples, so the volume fraction of spherical $Mg_{17}Al_{12}$ in PC samples is higher than that in NPC.

By analyzing the behavior of lamellar $Mg_{17}Al_{12}$ in samples versus the creep anisotropy, we found that the creep anisotropy is related to the volume fraction of this precipitates. During the creep deformation, dislocation slipping ordinarily occurred in the soft α-Mg grain interior, leading to large amounts of dislocations being piled up on the lamellar $Mg_{17}Al_{12}$, thereby causing strong stress concentration [16]. As a result, reticular β-$Mg_{17}Al_{12}$ skeleton is forced to disintegrate, consequently deteriorating the creep properties of samples [18]. Among the NPC samples, the basal slip NPC-TD sample contains the highest volume fraction of lamellar $Mg_{17}Al_{12}$, and this sample showed the worst creep performance. After pre-compression, although the Schmidt factor of the PC sample changed slightly since the high volume fraction of dynamic precipitates of spherical $Mg_{17}Al_{12}$ inhibited the basal slip of PC-TD sample. At the same time, spherical $Mg_{17}Al_{12}$ prevented the movement of dislocations and grain boundary during creep via pinning effect [34,35]. Therefore, contributed by pre-compression, the creep anisotropy was greatly improved to increase the volume fraction of the dynamic precipitates of spherical $Mg_{17}Al_{12}$.

4.2 Tensile fracture behavior

Figure 9 shows the creep fracture morphology of the NCP and PC samples under a stress of 60 MPa at 180 °C. With the limit of the slip system, Mg alloys usually undergo brittle fracture such as cleavage or quasi-cleavage fracture. In the case of the NPC-TD sample (Fig. 8(a)), minor cleavage fracture was observed, and some large and continuous cracks and holes were observed. Due to the fragile bonding at the Mg/$Mg_{17}Al_{12}$ phase interface [9,16], cracks are more likely to be generated in stress concentration due to the coarsening of lamellar $Mg_{17}Al_{12}$, so the NPC-TD sample with the most lamellar $Mg_{17}Al_{12}$ has a poor creep resistance. As shown in Fig. 9(b), the fracture of the NPC-ED sample showed striation besides cleavage fracture. This can be explained by the presence of a certain volume fraction of spherical

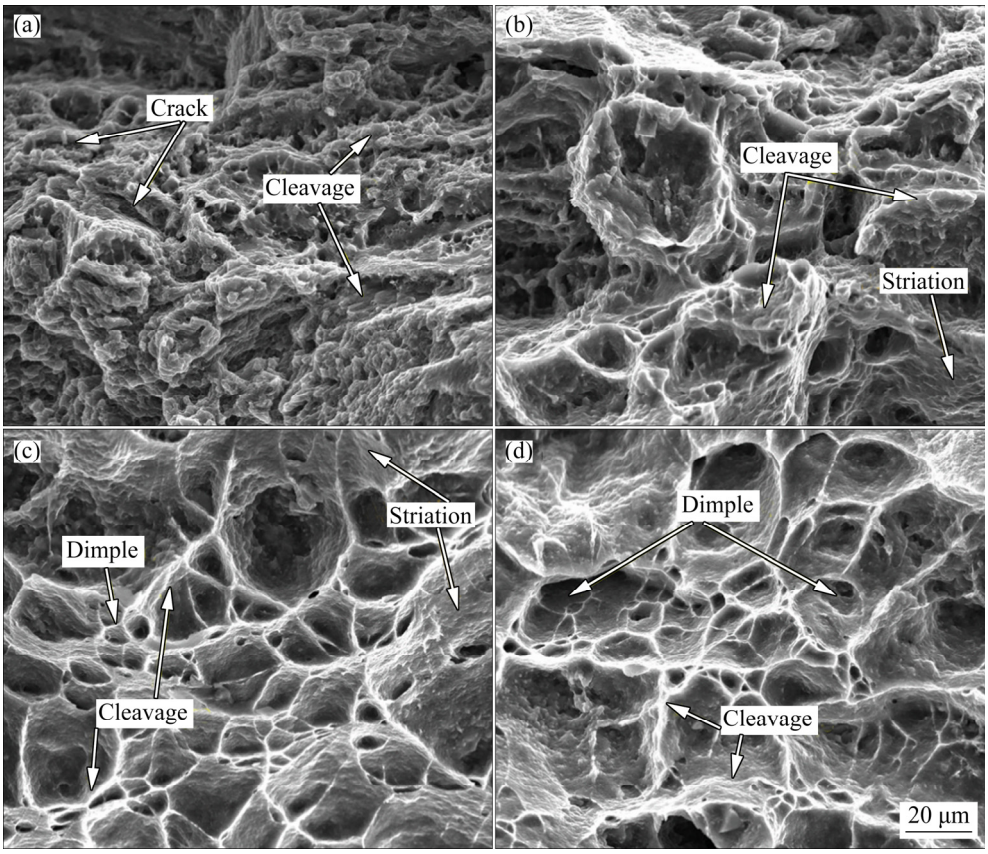

Fig. 9 SEM images of fracture surfaces after creep tensile testing of AZ91−2Y alloy in different directions: (a) NPC-TD; (b) NPC-ED; (c) PC-TD; (d) PC-ED

$Mg_{17}Al_{12}$ distributed at grain boundaries and within grains, with an dislocation slip resistance of the NPC-ED sample being enhanced as a result.

Figures 9(c, d) show the fracture morphologies of PC-TD and PC-ED samples, respectively. Compared with the NPC sample, the fracture surface of the PC sample contained a large number of cleavage planes and a certain number of dimples. Due to the lack of independent slip systems, especially at low deformation rates, twins played an important role in the plastic deformation mechanism of hexagonal-close-packed (hcp) metals, showing a positive effect on dislocation obstruction. On the other hand, the size of $Mg_{17}Al_{12}$ precipitates was reduced by the twins generated through pre-compression, increasing the number of spherical precipitates closely distributed within the grain, which hindered cleavage by trans-granular fracture. Therefore, the anisotropy of AZ91−2Y alloy was mostly improved by pre-compression through changing the volume fraction of spherical $Mg_{17}Al_{12}$ precipitates, which was consistent with the above results.

4.3 TEM analyses

In order to further study the influence of pre-compression on the anisotropy, TD samples with an obvious improvement in anisotropy were selected for TEM analysis. The bright-field TEM images under the two-beam mode of the NPC-TD and PC-TD samples, fractured under 60 MPa at 180 °C, are shown in Fig. 10. The incident beam direction for these images is $B=[11\bar{2}0]$ and two perpendicular diffraction directions $g=[01\bar{1}0]$ and [0002] are selected where ⟨*c*⟩ and ⟨*a*⟩ dislocations become invisible for $g\cdot B$ criterion, respectively [23]. A large number of lamellar $Mg_{17}Al_{12}$ precipitates can be seen in NPC-TD sample (Figs. 10(a−c)), and there is an obvious slip deformed regions in Fig. 10(a). Furthermore, as shown in Fig. 10(b), with $g=[01\bar{1}0]$, the majority of long and straight ⟨*a*⟩ dislocations become parallel to the traces of (0002) planes, as marked by the yellow-colored arrows, indicating that these dislocations are originated from the basal ⟨*a*⟩ slip. In Fig. 10(c), barely ⟨*c*⟩ dislocations can be seen with $\boldsymbol{g}=[0002]$, indicating that ⟨*c*⟩ dislocations are not activated and pyramidal ⟨*c*+*a*⟩ slip does not exist in NPC-TD sample. Thus, the dormitory creep mechanism for the NPC-TD sample is basal ⟨*a*⟩ slip.

For the PC-TD sample, twinning must be one of the creep mechanisms and it can be obviously seen from Figs. 10(d−f) that dynamic precipitation is mainly of spherical-type. In the direction of

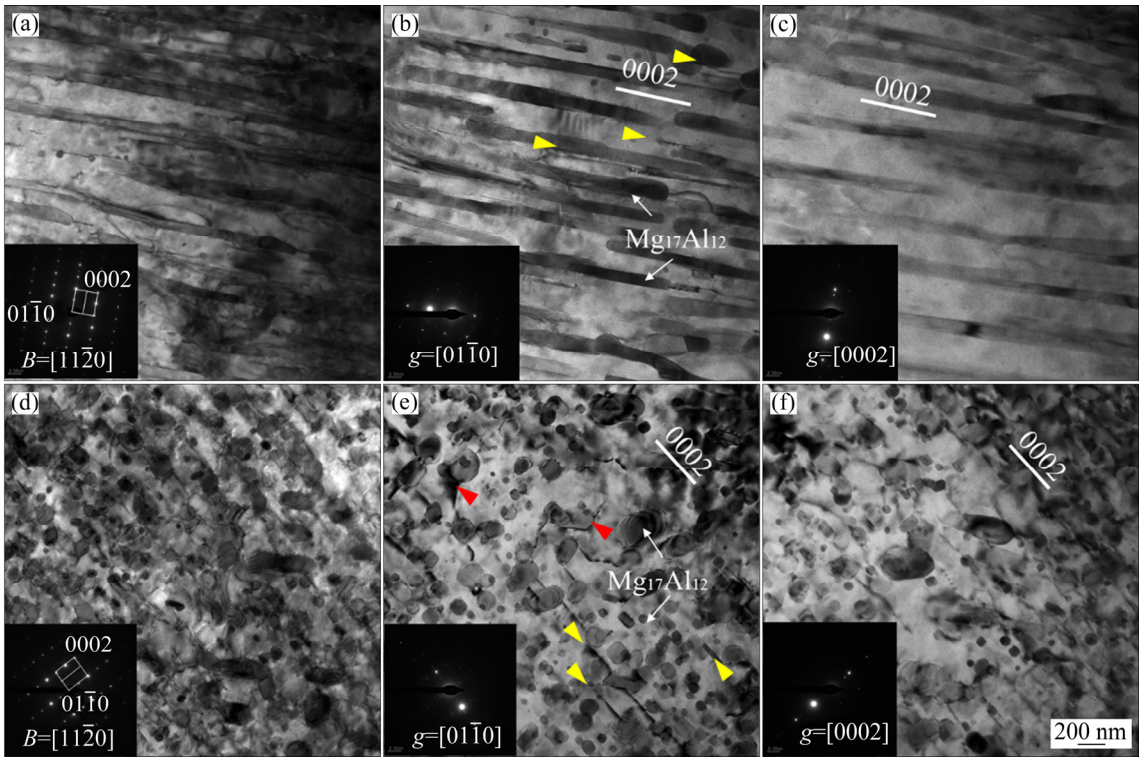

Fig. 10 Bright-field TEM images of NPC-TD (a, b, c) and PC-TD (d, e, f) samples fractured under 60 MPa at 180 °C

$g=[01\bar{1}0]$ (Fig. 10(e)), the basal $\langle a\rangle$ slip (marked by yellow-colored arrows) and prismatic $\langle a\rangle$ slip (marked by red-colored arrows) can be observed in PC-TD sample, so the cross-slip is activated during creep. A small amount of curly dislocations are presented and identified as $\langle c\rangle$ dislocations under $g=[0002]$ in Fig. 10(f), as a consequence of pyramidal $\langle c+a\rangle$ slip. Therefore, the creep mechanism of PC-TD specimen is cross-slip and twinning, accompanied by some pyramidal $\langle c+a\rangle$ slip. The activation of non-base slip greatly improved the creep resistance of PC-TD sample.

Overall, the pyramidal $\langle c+a\rangle$ slip is activated during the creep of PC samples after pre-compression. Combined with the above analysis, it can be considered that the dislocation mechanism is affected by the type of $Mg_{17}Al_{12}$ precipitates. The lamellar $Mg_{17}Al_{12}$ precipitates are parallel to the trace of (0002) planes in the NPC samples, facilitating the basal $\langle a\rangle$ slip and contributing to the rapid increase in creep strain. Instead, the spherical $Mg_{17}Al_{12}$ precipitates in the PC sample can hinder the movement of basal dislocations and activate the pyramidal $\langle c+a\rangle$ slip, resulting in dislocation entanglement and hardening to improve the creep resistance [33,36−38]. The creep anisotropy is greatly improved by increasing the amount of spherical $Mg_{17}Al_{12}$.

5 Conclusions

(1) The NPC samples showed an evident creep anisotropy at 180 °C. The NPC-TD samples showed the lowest creep resistance. After pre-compression, the creep resistance was sharply improved along the TD, and was slightly improved along the ED.

(2) Lamellar $Mg_{17}Al_{12}$ phases dynamically precipitated in NPC samples during the creep process. The more the amount of this precipitate is, the worse the creep resistance will be. PC samples precipitated spherical $Mg_{17}Al_{12}$ with a large volume fraction in the twin crystals. This large-volume-fraction spherical $Mg_{17}Al_{12}$ was mostly responsible for improving the creep anisotropy of AZ91−2Y alloy.

(3) The several types of $Mg_{17}Al_{12}$ precipitates contributed differently to the dislocation mechanisms. Thus, basal $\langle a\rangle$ slips were easily activated by lamellar $Mg_{17}Al_{12}$ found in large amounts in NPC samples. The spherical $Mg_{17}Al_{12}$ exerted a pinning effect mainly in PC samples, with the creep mechanisms being pyramidal $\langle c+a\rangle$ slips and twinning.

Acknowledgments

The authors acknowledge the financial support from the National Natural Science Foundation of China (Nos. 52075048, 52171099 and 52105140), the Natural Science Foundation of Hunan Province, China (No. 2021JJ40583), the Science and Technology Innovation Project of Hunan Province, China (No. 2018RS3073), the Scientific Research Innovation Project for Graduate Student of Changsha University of Science & Technology, China (No. CX2021SS55), and the Double First-class Scientific Research International Cooperation Project of Changsha University of Science and Technology, China (No. 2019IC15).

References

[1] HOU Cai-hong, YE Zhi-song, QI Fu-gang, WANG Qing, LI Lian-hui, OUYANG Xiao-ping, ZHAO Nie. Effect of Al addition on microstructure and mechanical properties of Mg−Zn−Sn−Mn alloy [J]. Transactions of Nonferrous Metals Society of China, 2021, 31: 1951−1968.

[2] FU Peng-huai, WANG Nan-qing, LIAO Hai-guang, XU Wen-yu, PENG Li-ming, CHEN Juan, HU Guo-qi, DING Wen-jiang. Microstructure and mechanical properties of high strength Mg−15Gd−1Zn−0.4Zr alloy additive-manufactured by selective laser melting process [J]. Transactions of Nonferrous Metals Society of China, 2021, 31: 1969−1978.

[3] CHEN Xia, ZHANG Ding-fei, ZHAO Yang, FENG Jing-kai, JIANG Bin, PAN Fu-sheng. Microstructure modification and precipitation strengthening for Mg−6Zn−1Mn−4Sn−0.5Ca through extrusion and aging treatment [J]. Transactions of Nonferrous Metals Society of China, 2020, 30: 2650−2657.

[4] TAHREEN N, CHEN D L, NOURI M, LI D Y. Influence of aluminum content on twinning and texture development of cast Mg−Al−Zn alloy during compression [J]. Journal of Alloys and Compounds, 2015, 623: 15−23.

[5] SRINIVASAN A, SWAMINATHAN J, GUNJAN M K, PILLAI U T S, PAI B C. Effect of intermetallic phases on the creep behavior of AZ91 magnesium alloy [J]. Materials Science and Engineering A, 2010, 527: 1395−1403.

[6] NAMI B, MIRESMAEILI S M, JAMSHIDI F, KHOUBROU I. Effect of Ca addition on microstructure and impression creep behavior of cast AZ61 magnesium alloy [J]. Transactions of Nonferrous Metals Society of China, 2019, 29: 2056−2065.

[7] LIANG Xin-li, PENG Xiang, JI Hao, LIU Wen-cai, WU Guo-hua, DING Wen-jiang. Microstructure and mechanical properties of as-cast and solid solution treated Mg−8Li−*x*Al−*y*Zn alloys [J]. Transactions of Nonferrous Metals Society of China, 2021, 31: 925−938.

[8] PENG Yong-gang, DU Zhi-wei, LIU Wei, LI Yong-jun, LI Ting, HAN Xiao-lei, MA Ming-long, PANG Zheng, YUAN Jia-wei, SHI Guo-liang. Evolution of precipitates in Mg−7Gd−3Y−1Nd−1Zn−0.5Zr alloy with fine plate-like 14H-LPSO structures aged at 240 °C [J]. Transactions of Nonferrous Metals Society of China, 2020, 30: 1500−1510.

[9] KHAN MD F, PANIGRAHI S K. Age hardening, fracture behavior and mechanical properties of QE22 Mg alloy [J]. Journal of Magnesium and Alloys, 2015, 3: 210−217.

[10] MAO Long-hui, LIU Chu-ming, GAO Yong-hao, HAN Xiu-zhu, JIANG Shu-nong, CHEN Zhi-yong. Microstructure and mechanical anisotropy of the hot rolled Mg−8.1Al−0.7Zn−0.15Ag alloy [J]. Materials Science and Engineering A, 2017, 701: 7−15.

[11] LI Zi-han, ZHOU Guo-wei, LI Da-yong, WANG Hua-miao, TANG Wei-qin, PENG Ying-hong, ZUROB H S, WU Pei-dong. Crystal plasticity based modeling of grain boundary sliding in magnesium alloy AZ31B sheet [J]. Transactions of Nonferrous Metals Society of China, 2021, 31: 138−155.

[12] WANG Chun-yu, ZHANG Yu-xiu, HUO Qing-huan, ZHANG Zhi-rou, TANG Jiao, HASHIMOTO A, YANG Xu-yue. Effects of twinning time node on the creep properties of dilute Mg−Y alloy [J]. Materials Science and Engineering A, 2021, 800: 140309.

[13] ZHANG Yu-xiu, HUO Qing-huan, ZHANG Zhi-rou, XIAO Zhen-yu, HASHIMOTO A, YANG Xu-yue. Anisotropy in the tensile creep behaviors of a hot-rolled Mg−5.5wt.%Y alloy sheet [J]. Materials Characterization, 2021, 172: 110843.

[14] LU J W, YIN D D, HUANG G H, QUAN G F, ZENG Y, ZHOU H, WANG Q D. Plastic anisotropy and deformation behavior of extruded Mg−Y sheets at elevated temperatures [J]. Materials Science and Engineering A, 2017, 700: 598−608.

[15] REN L B,QUAN G F, ZHOU M Y, GUO Y Y, JIANG Z Z, TANG Q. Effect of Y addition on the aging hardening behavior and precipitation evolution of extruded Mg−Al−Zn alloys [J]. Materials Science and Engineering A, 2017, 690: 195−207.

[16] ZHENG Liu-wei, NIE Hui-hui, LIANG Wei, WANG Hong-xia, WANG Yi-de. Effect of pre-homogenizing treatment on microstructure and mechanical properties of hot-rolled AZ91 magnesium alloys [J]. Journal of Magnesium and Alloys, 2016, 4: 115−122.

[17] ZHANG Dong-dong, LIU Chu-ming, JIANG Shu-nong, WAN Ying-chun, CHEN Zhi-yong. Effects of trace Ag on precipitation behavior and mechanical properties of extruded Mg−Gd−Y−Zr alloys [J]. Transactions of Nonferrous Metals Society of China, 2021, 31: 3394−3404.

[18] JIANG Bo, ZHANG Dong-dong, SUN Chi, LI Ning-xing, LIU Yong-bin, CAO Zhan-yi. Microstructure evolution and creep behavior of high-pressure die-cast Mg−9Al−1Zn−1Sr alloy [J]. Materials Science and Engineering A, 2019, 766: 138388.

[19] ZHA Min, ZHANG Hong-min, WANG Cheng, WANG Hui-yuan, ZHANG En-bo, JIANG Qi-chuan. Prominent role of a high volume fraction of Mg17Al12 particles on tensile behaviors of rolled Mg−Al−Zn alloys [J]. Journal of Alloys and Compounds, 2017, 728: 682−693.

[20] JIANG Ju-fu, LIN Xin, WANG Ying, QU Jian-jun, LUO Shou-jing. Microstructural evolution of AZ61 magnesium alloy predeformed by ECAE during semisolid isothermal treatment [J]. Transactions of Nonferrous Metals Society of China, 2012, 22: 555−563.

[21] XU Yan, HU Lian-xi, JIA Jian-bo, XU Bo. Microstructure evolution of a SIMA processed AZ91D magnesium alloy based on repetitive upsetting-extrusion (RUE) process [J]. Materials Characterization, 2016, 118: 309−323.

[22] ZHANG Dong-dong, YANG Shuo, MENG Fan-zhi, TIAN Zheng, XU Hong, CAO Zhan-yi, MENG Jian. Compressive creep behavior of extruded Mg−4Sm−2Yb−0.6Zn−0.4Zr alloy [J]. Materials Science and Engineering A, 2021, 809: 140929.

[23] XIAO Zhen-yu, HUO Qing-huan, ZHANG Zhi-rou, HUANG Wei-ying, LUO Lu, ZHANG Yu-xiu, HASHIMOTO Aki, YANG Xu-yue. Influence of pre-straining on creep behaviors of Mg−2Y alloy sheets [J]. Journal of Alloys and Compounds, 2019, 806: 19−32.

[24] CHEN Xiang, WANG Wei-zhang, ZHANG Jun-lei, HUANG Guang-sheng, LIU Shuai-shuai, TANG Ai-tao, JIANG Bin, PAN Fu-sheng. Tailoring AZ91 laminates for combination of strength and ductility [J]. Transactions of Nonferrous Metals Society of China, 2021, 31: 3703−3718.

[25] SHI Ya-feng, LUO Lu, HUO Qing-huan, WANG Jing, XIAO Zhen-yu, GUO Jun-cheng, YANG Xu-yue. Enhancing creep properties of a hot-rolled Mg−4Y binary alloy via a new thought of inhibiting cross-slip [J]. Materials Characterization, 2019, 147: 64−71.

[26] CHEN Hong-bing, LIU Tian-mo, LU Li-wei, HE Jie-jun, ZHAI Yan-bo. Influence of pre-strain and heat treatment on subsequent deformation behavior of extruded AZ31 Mg alloy [J]. Transactions of Nonferrous Metals Society of China, 2015, 25: 3604−3610.

[27] XIAO Zhen-yu, HUO Qing-huan, ZHANG Yu-xiu, ZHANG Zhi-rou, LI Ze-hao, HASHIMOTO A, YANG Xu-yue. Tensile creep anisotropy of a Mg−2Y alloy extruded sheet with a splitted texture [J]. Journal of Alloys and Compounds, 2020, 823: 153754.

[28] OUYANG Shu-xia, YANG Guang-yu, QIN He, LUO Shi-feng, XIAO Lei, JIE Wan-qi. High temperature creep behavior and creep microstructure evolution of T6 state Mg−15Gd alloy [J]. Materials Science and Engineering A, 2020, 780: 139138.

[29] HUANG Wei-ying, HUO Qing-huan, ZHANG Zhi-rou, TANG Jiao, HASHIMOTO A, YANG Xu-yue. Effects of original orientation on compressive creep behaviors of hot-extruded Mg−3Al−1Zn alloy rod [J]. Journal of Alloys and Compounds, 2019, 806: 1105−1108.

[30] WANG H, WANG Q D, BOEHLERT C J, YIN D D, YUAN J. Tensile and compressive creep behavior of extruded Mg−10Gd−3Y−0.5Zr (wt.%) alloy [J]. Materials Characterization, 2015, 99: 25−37.

[31] MO Ning, MCCARROLL I, TAN Qi-yang, CEGUERRA A, ZHANG Ming-xing. Understanding solid solution strengthening at elevated temperatures in a creep-resistant Mg−Gd−Ca alloy [J]. Acta Materialia, 2019, 181: 185−199.

[32] REED-HILL R E, ROBERTSON W D. The crystallographic characteristics of fracture in magnesium single crystals [J]. Acta Metallurgica, 1957, 5: 728−737.
[33] ZHANG Yu-xiu, XIAO Zhen-yu, HUO Qing-huan, ZHANG Zhi-rou, TANG Jiao, HASHIMOTO A, YANG Xu-yue. Effects of pre-compression on the three-dimensional creep anisotropy of a hot-rolled Mg−4wt.%Y binary alloy sheet [J]. Materials Science and Engineering A, 2020, 772: 138843.
[34] ROBSON J D, STANFORD N, BARNETT M R. Effect of precipitate shape on slip and twinning in magnesium alloys [J]. Acta Materialia, 2011, 59: 1945−1956.
[35] NIE Jian-feng. Effects of precipitate shape and orientation on dispersion strengthening in magnesium alloys [J]. Scripta Materialia, 2003, 48: 1009−1015.
[36] LI Jing, WU Jia-lin, Li Jin, MERT C, WANG Feng-hua, DONG Shu-ai, DONG Jie. The role of dislocation−solute interactions on the creep behaviour of binary Mg−RE alloys [J]. Scientific Reports, 2021, 11: 2860.
[37] HUANG Wei-ying, CHEN Jian-hua, ZHANG Rui-zhi, YANG Xu-yue, JIANG Li-ping, XIAO Zhen-yu, LIU Ya-qun. Effect of deformation modes on continuous dynamic recrystallization of extruded AZ31 Mg alloy [J]. Journal of Alloys and Compounds, 2021, 897: 163086.
[38] HU Yi-xie, SUN You-ping, HE Jiang-mei, FANG De-jun, ZHU Jia-xin, MENG Xiang-chao. Effect of friction stir processing parameters on the microstructure and properties of ZK60 magnesium alloy [J]. Material Research Express, 2022, 9: 016508.

预压缩对热挤压 AZ91−2Y 镁合金动态析出相形成及蠕变各向异性的影响

李 微[1]，黄 煌[1]，黄伟颖[1]，陈 荐[1]，张圣德[2]，肖振宇[3]，邱 玮[1]

1. 长沙理工大学 能源与动力工程学院 高效清洁能源利用重点实验室，长沙 410114；
2. Japan Electric Power Central Research Institute, Tokyo 240-0196, Japan;
3. 湖南大学 汽车车身先进设计制造国家重点实验室，长沙 410082

摘 要：研究经预压缩(PC)和未经预压缩(NPC)的热挤压 AZ91−2Y 镁合金在 180 °C 不同应力下的蠕变各向异性行为。采用扫描电子显微镜(SEM)、电子背散射衍射(EBSD)、透射电子显微镜(TEM)和拉伸蠕变试验对合金的显微组织、织构和力学性能进行分析。结果表明，抗蠕变性能与球形 $Mg_{17}Al_{12}$ 析出相的体积分数成正比。NPC 试样中动态析出高体积分数层片状 $Mg_{17}Al_{12}$，使其以基面⟨*a*⟩滑移为主导蠕变机制，且 NPC 试样具有明显的各向异性。PC 试样动态析出高体积分数的球形 $Mg_{17}Al_{12}$，对基面⟨*a*⟩滑移有抑制作用。锥面⟨*c*+*a*⟩滑移和孪晶显著提高蠕变各向异性抗力。

关键词：镁合金；蠕变各向异性；预压缩；孪晶；位错

(Edited by Bing YANG)